Ten-Minute Sea-Level Variations From Combined Multi-GNSS Multipath Reflectometry Based on a Weighted Iterative Least-Square Method

Mingda Ye, Shuanggen Jin, *Senior Member, IEEE*, and Yan Jia, *Member, IEEE*

***Abstract*— Accurate and high-frequency sea-level monitoring is of great importance in ocean environments and global climatic studies, but traditional techniques have their respective limitations. In the last decades, the application of Global Navigation Satellite System Multipath Reflectometry (GNSS-MR) in sea-level monitoring has developed rapidly. Recently, more available GNSS signals are expected to bring new opportunities to improve its performance and achieve high spatial–temporal resolution. In this article, a new algorithm is developed to optimize the method of multi-GNSS multipath reflectometry and improve the precision and sampling rate for GNSS-MR sea-level monitoring. In order to make full use of the short-term multipath oscillation information, a sliding window is used to collect the signal-to-noise ratio (SNR) sequences. A weighted iterative least-square method is introduced to combine the selected SNR observations of GPS, GLONASS, Galileo, and BDS systems and retrieve sea level at 10-min intervals at BRST station for one year. A novel index called local kurtosis (LK) is proposed, which can be used to evaluate the quality of the Lomb–Scargle periodogram (LSP) and design the weight matrix in the least-square combinatorial process. Compared to using individual signals, the optimized combination algorithm decreased the root mean square error (RMSE) by 78%, from 0.610 to 0.134 m, and increased the correlation coefficient R^2 from 0.851 to 0.992. In addition, the tidal constituents monitored by multi-GNSS-MR and tide gauge are highly consistent, demonstrating that the multi-GNSS-MR can accurately retrieve daily and subdaily tidal constituents of periods longer than 10 min.**

***Index Terms*— Global Navigation Satellite System Multipath Reflectometry (GNSS-MR), sea level, signal-to-noise ratio (SNR), tidal constituent, weighted iterative least-square method.**

I. Introduction

GLOBAL warming has been receiving increasing attention since the late last century, mainly due to the apparent rise in global sea level caused by the increase in temperature, which is promised to make a great impact on the coastal area where a large amount of the population gathers [1], [2]. In this case, accurate sea level and tidal information has become more important in ocean environments and climate change research [3]. Traditional techniques for sea-level measuring, such as tide gauge and satellite altimetry, have their respective advantages and disadvantages. Tide gauges have high precision and high sampling frequency, but only provide *in situ* and relative sea-level observation. In this case, tide gauges are susceptible to vertical land movements, and need the co-located geodetic GNSS sites to provide absolute sea level. Satellite altimetry provides absolute sea-level variation, but it has a low sampling rate, and the contamination of radar signals by land makes it difficult to obtain sea level in coastal areas [4], [5]. Therefore, traditional techniques cannot meet the demand of all-time, all-weather, and high spatial–temporal sampling. Therefore, a new technique known as Global Navigation Satellite System Multipath Reflectometry (GNSS-MR) was introduced [6].

In the last decades, extensive works about ground-based GNSS-MR have demonstrated that the sea level can be retrieved using a single coastal GNSS receiver [7]–[10]. GNSS-MR works by extracting the multipath oscillations from GNSS observations and analyzing the reflector information on the interference pattern of the direct and reflected signal. Martin-Neira [11] presented the concept of combining the direct and reflected GPS signals to remotely sense the sea surface change. Thereafter, Anderson [12], [13] proposed the concept of GPS tide gauge and the commonly used the signal-to-noise ratio (SNR) method. Bilich and Larson [14] further presented a power spectral mapping tool to retrieve the GPS multipath environment using SNR observation. Recently, lots of studies focus on optimal methods of multi-GNSS multipath reflectometry. Tabibi *et al.* [15] analyzed the statistical characteristics for each signal of GPS and GLONASS and tested the performance of intersignal combination retrieving. Jin *et al.* [8] analyzed the performance of BDS-R using triple-frequency SNR, pseudo-range, and carrier phase. Santamaría-Gómez and Watson [16] processed the SNR series using an extended Kalman smoother and allowed GNSS-MR to detect small but significant changes in SNR oscillation. Zheng *et al.* [17] compared the accuracy of different SNR types and analyzed the monitoring effect of BDS2-IGSO, BDS2-MEO, and BDS3-MEO [17]. Several previous pieces of research also focused on correcting the tropospheric delay, which is one of the significant error sources in GNSS-MR. Treuhaft *et al.* [18]

Manuscript received 20 February 2022; revised 27 April 2022 and 17 June 2022; accepted 15 July 2022. Date of publication 26 July 2022; date of current version 5 August 2022. This work was supported in part by the Chinese Academy of Sciences through the Strategic Priority Research Program Project of under Grant XDA23040100, in part by the Jiangsu Natural Resources Development Special Project under Grant JSZRHYKJ202002, and in part by the Shanghai Leading Talent Project under Grant E056061. *(Corresponding author: Shuanggen Jin.)*

Mingda Ye is with the Shanghai Astronomical Observatory, Chinese Academy of Sciences, Shanghai 200030, China, and also with the School of Astronomy and Space Science, University of Chinese Academy of Sciences, Beijing 100049, China (e-mail: mdye@shao.ac.cn).

Shuanggen Jin is with the Shanghai Astronomical Observatory, Chinese Academy of Sciences, Shanghai 200030, China, and also with the School of Surveying and Land Information Engineering, Henan Polytechnic University, Jiaozuo 454000, China (e-mail: sgjin@shao.ac.cn).

Yan Jia is with the Department of Surveying and Geoinformatics, Nanjing University of Posts and Telecommunications, Nanjing 210023, China.

Digital Object Identifier 10.1109/TGRS.2022.3194033

used a mapping function to estimate the altimetric height of zenith tropospheric delay for correction. Williams and Nievinski [19] compared the results of tropospheric correction at 20 different GNSS coastal stations (including BRST station) using different methods.

However, there still exist several defects in the current technique. For example, the temporal resolution of traditional methods is mostly worse than 1 h. Moreover, most recent studies did not fully utilize the periodogram as a quality indicator, which may cause precision decline. Therefore, a new algorithm is proposed in this article to realize high precision and robust retrieval performance at a 10-min interval. The basic theory of the SNR method is introduced in Section II-A. Then, the algorithm details designed to improve time resolution and inversion precision are described in Section II-B. Section II-C presented the situation about station BRST, the signal selection, and the settings for azimuth and elevation limitation. Results of the experiment are visualized and comparatively analyzed in Section III, where a tidal harmonic analysis is performed to refine the validation of GNSS-MR retrieving performance (Section III-C).

II. Methods and Data

A. Method of GNSS SNR-Based Altimetry

SNR is one of the main observables of GNSS, which has been used generally in assessing signal quality as the ratio of signal power to noise power. The multipath effect can cause oscillations in SNR observations, which makes it possible to retrieve physical information about the reflective surface, that is, snow depth and sea level [20]. Nievinski and Larson [21] presented the multipath forward model, the simplified expression of SNR is described as

$$\begin{cases} \mathrm{SNR} = t\mathrm{SNR} + \delta\mathrm{SNR} \\ t\mathrm{SNR} = \left(P_d + P_r + P_r^I\right) P_n^{-1} \\ \delta\mathrm{SNR} = 2\sqrt{P_d}\sqrt{P_r}P_n^{-1}\cos\varphi_i \end{cases} \tag{1}$$

where tSNR is the sum of trends, and δSNR is the sum of detrended interference fringes. P_d is the direct power, P_r is the reflected power, pn is the noise power, and P_r^I is the incoherent power, while $\varphi_i = \varphi_r - \varphi_d$ is the interferometric phase of the direct phase ϕ_d and the reflected phase ϕ_r. The interference fringe causes multipath oscillation in SNR observations, and therefore, multipath patterns can be obtained after detrending SNR series using low-order polynomial fitting (second order in this article).

Assuming that the sea surface is a planar reflector, the relative phase angle Ψ can be derived in terms of the difference in propagation distance between direct and reflected signal Δ as

$$\Psi = \frac{2\pi}{\lambda}\Delta = \frac{4\pi h}{\lambda}\sin\varepsilon \tag{2}$$

where h is the reflector height (RH) defined as the nonstatic height of the receiver's antenna phase center above the ground surface (see Fig. 1), λ is the wavelength of GNSS signal, and ε is the elevation angle of satellites. Then, the frequency of

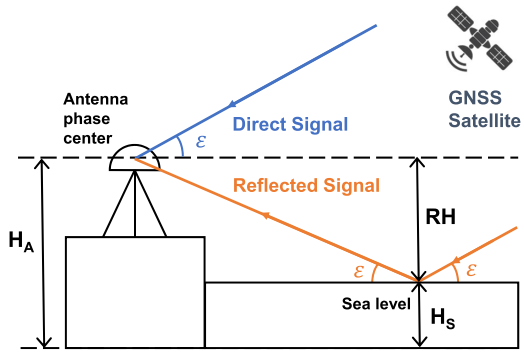

Fig. 1. Geometry of reflected GNSS signals.

the multipath oscillation can be obtained as

$$f = \frac{d\Psi}{dt} = \frac{4\pi h}{\lambda}\cos\varepsilon\frac{d\varepsilon}{dt}. \tag{3}$$

Larson *et al.* [22] found that a height change rate correction was significant for stations where the sea surface changed drastically. Taking the change rate $\dot{h} = (dh/dt)$ into account, (3) can be rewritten as

$$f = \frac{4\pi\dot{h}}{\lambda}\sin\varepsilon + \frac{4\pi h}{\lambda}\cos\varepsilon\frac{d\varepsilon}{dt}. \tag{4}$$

Using sine of the elevation angle as the independent variable, the frequency of multipath oscillation with respect to $x = \sin\varepsilon$ is written as

$$f_x = \frac{d\Psi}{dx} = \frac{4\pi}{\lambda}\left(\dot{h}\frac{\tan\varepsilon}{\dot{\varepsilon}} + h\right). \tag{5}$$

The multipath frequency modulates δSNR can be written as [23]

$$\delta\mathrm{SNR} = A\cos\left(\frac{4\pi\overline{h}}{\lambda}\sin\varepsilon + \varphi\right) = A\cos(2\pi f_x x + \varphi) \tag{6}$$

where $\overline{h}$ is the RH obtained in static assumption, A is the oscillation amplitude, and φ is the phase offset. To obtain the dominant frequency requires uneven discrete spectrum analysis on account of the unequally spaced elevation angle series. Lomb and Scargle presented a spectral analysis method, Lomb–Scargle periodogram (LSP). LSP can calculate the spectral power of specified frequency for irregularly spaced time series [24], [25]. Using LSP, δSNR data are transferred to the frequency domain, and the main frequency f_x can be obtained. Then, the static RH is retrieved as

$$\overline{h} = \frac{f_x \cdot \lambda}{2} = \dot{h}\frac{\tan\varepsilon}{\dot{\varepsilon}} + h. \tag{7}$$

Then, the geocentric sea level is retrieved as $h_S = h_A - h$ with h_A representing the antenna phase center height above the ellipsoid (see Fig. 1).

B. Data Processing

As shown in the flowchart (see Fig. 2, step 1), the downloaded 1-Hz GNSS observation data will be processed using single point positioning, which calculates elevation and azimuth angles for each satellite at each observation epoch.

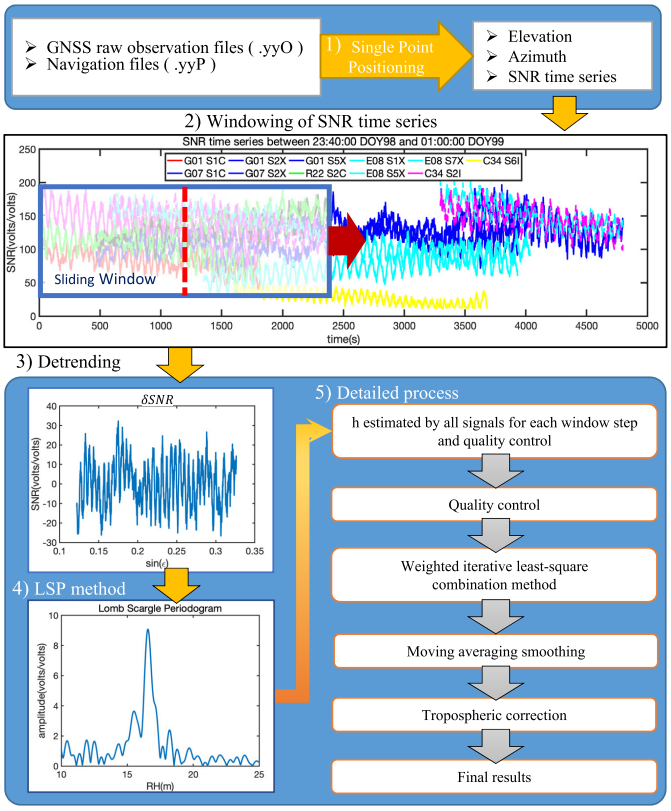

Fig. 2. Processing flowchart.

The elevation, azimuth, and SNR time series are then obtained and go to steps 2–5.

1) Windowing of the SNR Time Series: In previous research, Roussel *et al.* [9] have analyzed the performance of the moving time window, but the window is used to separate RH estimations retrieved for each satellite track. However, there are two drawbacks to this method. First, a single satellite track might cover several hours, and the frequency of the oscillation changes during the period. Larson *et al.* [7] divided a long track into a rising arc and a setting arc, and the result shows that the RH retrieved by these two arcs differs over 1 m from each other. Although the change rate of height can be estimated, the commonly used linear model is not able to prevent large errors when a satellite track is too long. Second, for the same reason that one track only generates one or two (when divided into a rising arc and a setting arc) estimations, high-frequency retrieval is hard to realize in poor observation conditions.

To obtain information with a higher temporal resolution, a sliding window that directly separates SNR time series into fragments of uniform width and interval is adopted (see flowchart step 2). The width is set to 40 min and the interval is 10 min in this article. The segmented SNR time series longer than 300 s within the window are then converted to static RH estimations and quality-controlled. Note that for each simultaneously observed signal (of different satellites and channels), different $\overline{h}$ values are estimated separately.

2) Quality Control: The segmented SNR time series are detrended using a second-order polynomial fitting, and the δSNR time series are converted to the frequency domain using the LSP method. Then, the dominant frequency and the corresponding RH estimation can be determined. To optimize the quality of raw RH estimations, several thresholds are set to reject detrimental values and outliers.

TABLE I
QUALITY CONTROL CRITERIA

Item	*Strategies*
Peak amplitude	$A_p > 7volts$
Reflector height	$10m < RH < 25m$
Peak-to-noise ratio	$PRN > 3$
Outlier elimination	*IQR checking (Eq.10)*

First, having used LSP to transfer SNR series from the time domain to the frequency domain, the frequency of the most significant spectral peak will be selected as the dominant frequency. To prevent extreme outliers, the corresponding static RH is based on (7) and restricted between 10 and 25 m. Besides, to prevent the effect of multipeak situations where spectral power is dispersive, the minimum threshold of the peak amplitude is set to 7 V.

The peak-to-noise ratio (PNR) is universally used as the major index for evaluating the quality of LSP defined as [22], [26], [27]

$$\mathrm{PNR} = \frac{A_p}{\overline{A}} \tag{8}$$

where A_p is the amplitude of peak frequency, and $\overline{A}$ is the mean amplitude of all frequency points within the established range. In this article, peaks with PNR larger than 3 are considered significant, and the corresponding RH estimations are then calculated based on (7). To further eliminate the detriment of outliers while facilitating the comparative analysis of different signals, the primary estimations are classified by observation codes and processed, respectively. The interquartile range (IQR) is calculated for each class as (9), and values within the range defined by (10) will be considered outliers

$$\mathrm{IQR} = Q3 - Q1 \tag{9}$$

$$x_{\mathrm{outlier}} = \{x | x \le Q1 - 1.5 * \ \mathrm{IQR} \text{ or } x \ge Q3 + 1.5 * \mathrm{IQR}\} \tag{10}$$

where $Q1$ is the first quartile and $Q3$ is the third quartile. This criterion is commonly used in statistical analysis, the statistical graph based on this method is called a boxplot. Table I presents all the quality control criteria.

3) Weighted Iterative Least-Square Method: The standard least-squares method (LSM) has been proved to have outstanding performance in combining estimations of several GNSS satellites in a selected epoch to determine RH. Previous research made by Roussel *et al.* [9] conjointly determined nonstatic RH and change rate $\dot{h}$ using standard LSM where the weight matrix is not specially designed. Wang *et al.* [28] presented a robust regression strategy which is a kind of

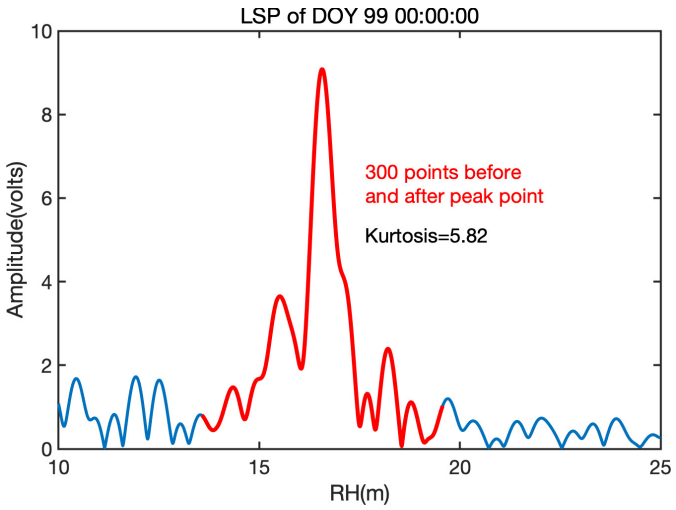

Fig. 3. Data points for calculating LK in an LSP diagram.

dynamic LSM, and it continuously updates the weight matrix based on the posterior residuals of the latest iteration.

The observation equation of the LSM is according to (7). When n static RH estimations are selected, it can be expressed as

$$\begin{pmatrix} \cdots \\ \bar{h}_{pq}(t) \\ \cdots \end{pmatrix} = \begin{pmatrix} \cdots & \cdots \\ 1 & \frac{\tan \varepsilon_p}{\dot{\varepsilon}_p} \\ \cdots & \cdots \end{pmatrix} \begin{pmatrix} h(t) \\ \dot{h}(t) \end{pmatrix} \tag{11}$$

where p is the satellite, q is the observation code, and t is the epoch of observation. It is equivalent to the matrix equation as follows:

$$L_{n\times 1} = B_{n\times 2}\hat{X}_{2\times 1} \tag{12}$$

where $\hat{X}$ is solved with the traditional LSM equation

$$\widehat{X} = \left(B^T P B\right)^{-1} B^T P L \tag{13}$$

where P is the weight matrix. In this article, a quality indicator called local kurtosis (LK) is introduced to set the weight value. The LK of an LSP diagram is the kurtosis of a specific number (set as an empirical value of 300 in this article) of data points before and after the peak frequency data point, which can represent the sharpness of the peak (see Fig. 3). The sharper the peak, the greater the kurtosis and the higher the retrieval quality. Hence, the weight matrices are designed based on the corresponding LK values of RH estimations. To find the most suitable weight values, an exponential function is adopted as the way to tune the degree of distinction between estimations with different LK values. The weight value is set to

$$P_i = \frac{\mu^{k_i}}{\nu} \tag{14}$$

where P_i and k_i are the weight and LK value of the ith estimation in L, respectively; μ is the base, and ν is the scale factor, where both are constants. Testing with part of the data yields optimal settings for both hyperparameters.

To minimize the error, multiple iterations are performed. For each iteration, the process is expressed as

$$\widehat{X}^{(i+1)} = \left(B^T P B\right)^{-1} B^T P L^{(i)} \tag{15}$$

where i represents the current iteration count. Then, $B\widehat{X}$ will be assigned to L. The iteration continues until the change of $\widehat{X}$ meets the condition

$$\|\widehat{X}^{(i+1)} - \widehat{X}^{(i)}\| < \delta. \tag{16}$$

The estimations of nonstatic RH and change rate $\dot{h}$ for each window epoch are then obtained.

To weaken the effect of accidental error and facilitate the following tropospheric correction, a moving average process is conducted at 10-min intervals on the nonstatic RH time series. The width of the averaging window is four epochs, that is, 40 min, the same as the SNR window width.

4) Tropospheric Correction: In previous research, Santamaría-Gómez mentioned that tropospheric refraction would bend the signals and lead to a higher elevation angle, thus a larger geometric delay will be calculated, and results in a larger estimation of RH [29]. Therefore, a simplified scale correcting method is used to reduce the impact of tropospheric delay in this article. Williams and Nievinski [19] pointed out that tropospheric delay can be processed as a scale error as (17) and the simplified equation of RH considering tropospheric correction is as (18)

$$h_{\text{tropo}} = \alpha\left(\widehat{h}_A - \widehat{h}_S\right) = \alpha\widehat{h} \approx \alpha h \tag{17}$$

$$\widehat{h} = \widehat{h}_A - \widehat{h}_S = h + h_{\text{tropo}} \tag{18}$$

where $\widehat{h}$, $\widehat{h}_A$, and $\widehat{h}_S$, respectively, represent the actual value of RH, antenna height, and sea level. h is the calculated estimation of nonstatic RH, and α is the scale factor of the tropospheric correction related to the RH. Rearranging (17) and (18), we get the corrected RH

$$\widehat{h} = \frac{h}{(1+\alpha)} \tag{19}$$

where α is the scale factor of the nonstatic RH. Besides, Larson *et al.* [22] demonstrated that if the reflector surface is moving, the RH estimations will bias. Therefore, as the sea surface keeps changing in height, another scale error depending on the sea level change rate can be used to correct tropospheric delay conjointly with the abovementioned one. The final correcting equation is

$$\widehat{h} = \frac{h}{(1+\alpha)} + \beta\dot{h} \tag{20}$$

where β is the scale factor of the sea level change rate. The factors α and β can be determined using a least-square estimation (independent of the LSM model in the last subsection) based on *a priori* data. When n epochs of *a priori* data are used, the observation equation is expressed as

$$\begin{pmatrix} \cdots \\ \widehat{h}(t) \\ \cdots \end{pmatrix} = \begin{pmatrix} \cdots & \cdots \\ h(t) & \dot{h}(t) \\ \cdots & \cdots \end{pmatrix} \begin{pmatrix} \frac{1}{(1+\alpha)} \\ \beta \end{pmatrix} \tag{21}$$

and the matrix form is the same as (12). The factors α and β are then determined with (13), which can be used to correct the tropospheric delay of the pending data.

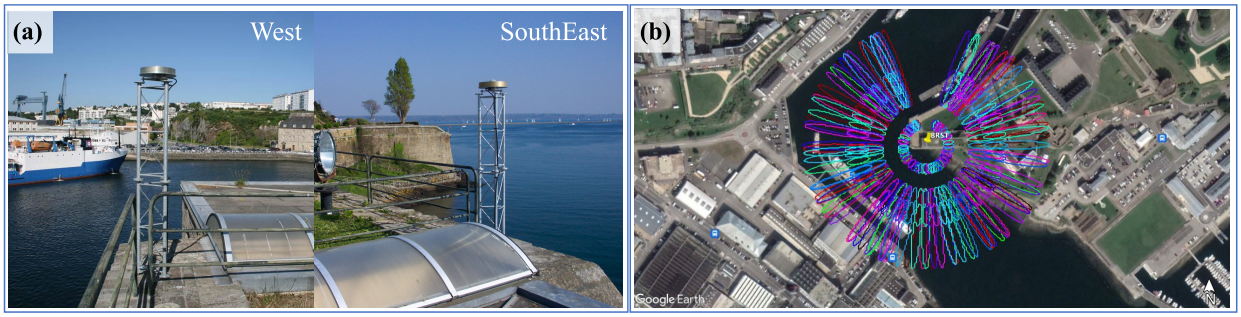

Fig. 4. (a) Antenna of station BRST in France (https://igs.org/imaps/station.php?id=BRST00FRA). (b) First Fresnel zones of elevation angles 7°, 10°, and 25° at station BRST projected on Google Earth.

TABLE II
BRIEF CHARACTERS OF SELECTED SIGNALS

Satellite system	*Frequency band*	*Frequency / Hz*	*Observation code*
GPS	*L1*	*1575.42*	*S1C*
	L2	*1227.60*	*S2X*
	L5	*1176.45*	*S5X*
GLONASS	*G1*	*1602+k*9/16 (k= -7 ... +12)*	*S1C*
	G2	*1246+k*7/16*	*S2C*
Galileo	*E1*	*1575.42*	*S1X*
	E5a	*1176.45*	*S5X*
	E5b	*1176.45*	*S7X*
BDS	*B1-2*	*1561.098*	*S2I*
	B3	*1268.52*	*S6I*
	B2b	*1207.140*	*S7I*

C. Data

The Multi-GNSS Experiment (MGEX) project was set up by International GNSS Service (IGS) to track, collate, and analyze all available GNSS signals [30]. The MGEX station BRST, which locates at the mouth of Penfeld River in Brest, France, is selected to estimate the sea level. The station was equipped with a TRIMBLE ALLOY receiver and TRM57971.00 antenna [see Fig. 4(a)], providing multisystem high-rate observation data with a 1-s sampling interval. The station is only 292 m away from the Brest tide gauge; the posterior validated sea level data recorded at 10-min sampling intervals by the tide gauge can be accessed at the data archive run by tidal observation reference networks of France (Réseaux de référence des observations marégraphiques, REFMAR, http://data.shom.fr/donnees/refmar).

In this article, the SNR data of a whole 2021 (DOY 1–365) is used to study the annual performance of GNSS-MR and its ability to retrieve astronomical tidal constituents. Previous research [28] experimentally analyzed the retrieval performance for each signal in four systems and verified the precision of raw single signal GNSS-MR. Within the GPS L2 band, S2X has a significant advantage compared to S2W. Galileo S1X, S5X, and S7X have relatively better performance. GLONASS S1C and S2C have similar precision to S1P and S2P. After taking calculated efficiency and performance into account, the selected signals in this article are shown in Table II.

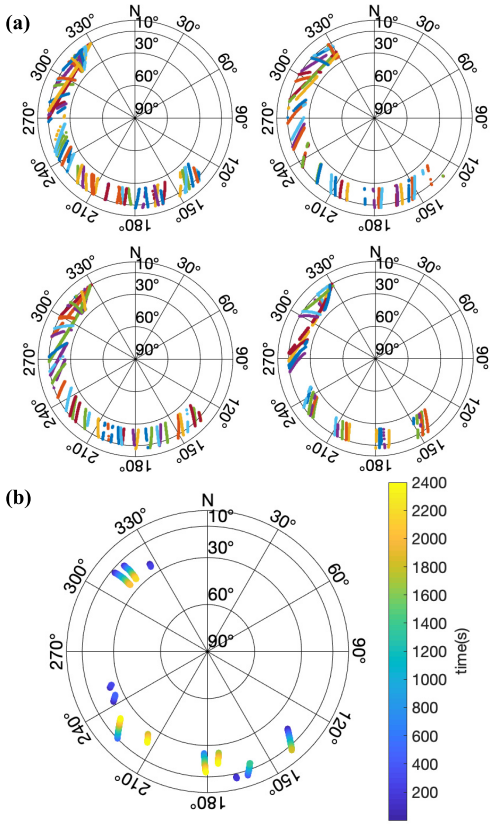

Fig. 5. (a) Selected satellite tracks of DOY 99 for four systems [(Top left) GPS. (Top right) GLONASS. (Bottom left) Galileo. (Bottom right) BDS]. (b) Selected satellite tracks of a window (00:00:00–00:40:00) in DOY 99.

To determine the masks of elevation and azimuth angle in the study, the First Fresnel Zones of elevation angle 7°, 10°, and 25° with RH set to 16 m for station BRST are plotted using an open-sourced MATLAB/Octave tool in GPS-toolbox developed by Roesler and Larson [31]. As shown in Fig. 4(b), the area with azimuths ranging from 130° to 180° is an open water area, and an elevation range of 7°–25° is selected. Azimuths ranging from 180° to 330° are within the narrower Penfeld River, and the elevation mask is restricted to 10°–25°. The selected satellite tracks in DOY 99 for four systems are plotted [see Fig. 5(a)], showing that different systems all provided a sufficient number of tracks with good continuity. Furthermore, to present the situation after windowing, a sample of the segmented satellite tracks in one window is plotted in Fig. 5(b).

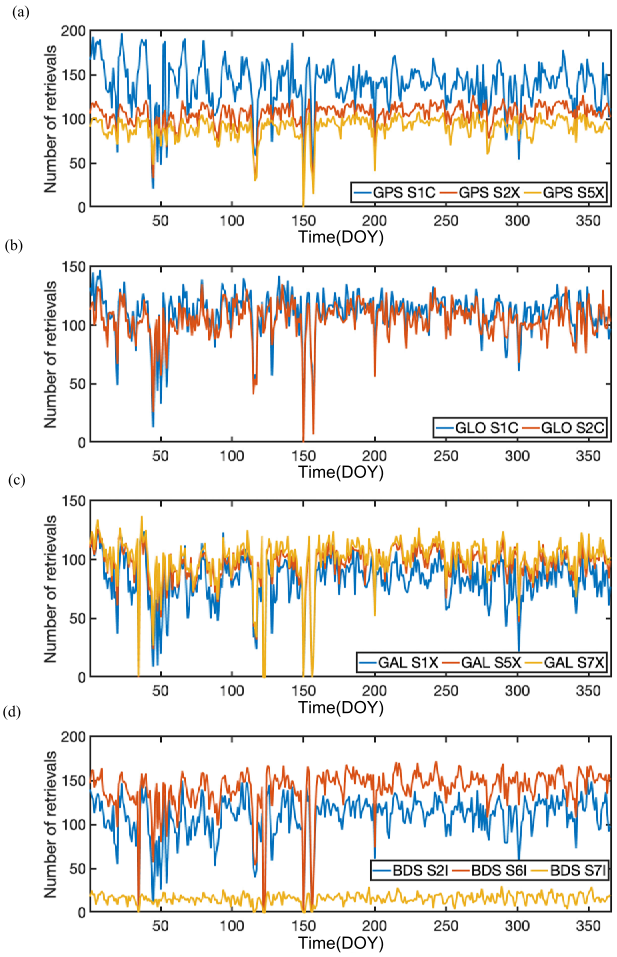

Fig. 6. Number of valid retrievals per day for each signal. The unit of the time axis is the day of the year (DOY). (a) GPS. (b) GLONASS. (c) Galileo. (d) BDS.

III. Results and Analysis

A. Performance of Individual Signal

Before the combinative process, a comparative analysis is conducted to evaluate the performance of different signals according to the following indicators: valid retrievals per day, root mean square error (RMSE), and correlation (R^2). Fig. 6 shows the number of valid retrievals per day for each SNR type of the four systems during the whole 365 days in 2021. Note that the number of valid retrievals on someday is very low, for example, DOY 35, 122, 123, 150, and 157, due to several observation interruptions at the BRST station. In addition, the BDS-3 B2b signal is not received by the receiver, resulting in only 15.9 valid retrievals per day for S7I. The average numbers of valid retrievals per day for each signal are shown in Table III, which indicates that GPS S1C and BDS S6I provided the most valid retrievals around 140 per day, and all normally received SNR types provided more than 80 valid retrievals per day, which were mainly due to the direct segmentation of the SNR time series.

Table III also presents the RMSE of raw estimations for each SNR type. GLONASS S1C has the best precision at 0.513 m, while Galileo S7X has the worst at 0.693 m. To present the

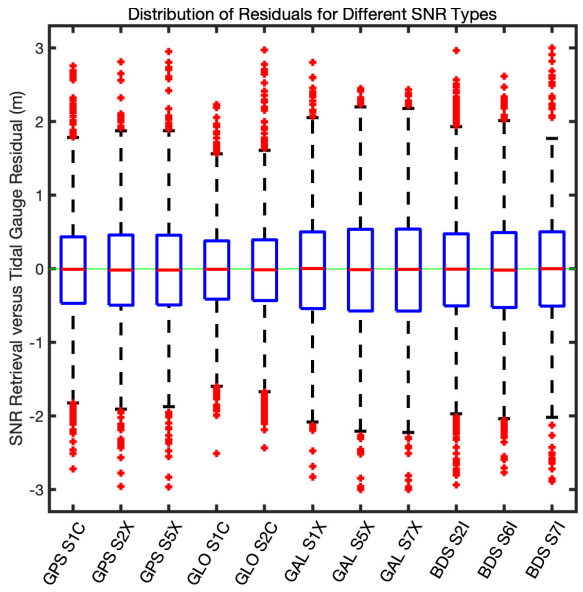

Fig. 7. Distribution of residuals for each SNR type.

residual distribution for each SNR type more clearly, a boxplot is drawn in Fig. 7, where the blue box represents the range between the first and third quartiles and the red horizontal lines represent the medians. The outlier criteria settings are the same as in (7), and the red crosses represent outliers based on this criterion. The results of the quartile analysis are almost the same as those of the RMSE analysis, except that the residuals of BDS S7I seem to be more convergent in the quartile analysis than those of S6I.

When evaluating the performance of different SNR types, RMSE and the number of retrievals should be considered together. Among GPS signals, S2X and S5X have the highest precision, and S1C provided the most retrievals. In terms of GLONASS, S1C has the highest precision and provided the most retrievals as well. S1X is the most precise in Galileo, while S7X provided the most retrievals. As for BDS, S2I and S6I have almost the same precision but S6I provided the most retrievals. Overall, in comparison between systems, the performance ranking is GLONASS > GPS > BDS > Galileo, which is consistent with previous researches [15], [17], [28].

Fig. 8 shows the correlation analysis charts of tide gauge and GNSS-MR retrievals for GPS, GLONASS, Galileo, and BDS. The solid red line is the linear fit line and the red dotted line is the 95% confidence interval line. The corresponding parameters including the goodness of fit R^2 and coefficients a and b in linear form $y = ax + b$ are shown in Table III, where a is replaced by slope deviation $(a - 1)$ to demonstrate the subsequent improvement. The result of the linear fitting is quite consistent with the result of RMSE analysis, which shows that GLONASS S1C has R^2 and a closer to 1 and its b is much less than others. Also, the fitting goodness identically ranks GLONASS > GPS > BDS > Galileo. It is worth noting that all R^2 and a less than 1 and all b larger than 0, which means that the deviation direction of the fitting curve is uniform and systematic. This is most likely because

TABLE III

NUMBER OF VALID RETRIEVALS PER DAY, RMSE, $R2$, LINEAR COEFFICIENTS (A-1, B) FOR EACH SNR TYPE

Observation code	*The average number of valid retrievals per day*	*RMSE(m) (Raw retrieval)*	R^2	*a-1(m/m)*	*b(m)*
GPS-S1C	138.3	0.578	0.886	-0.113	0.487
GPS-S2X	105.0	0.595	0.883	-0.117	0.502
GPS-S5X	90.5	0.596	0.881	-0.118	0.506
GLONASS-S1C	109.8	0.513	0.911	-0.088	0.376
GLONASS-S2C	104.7	0.534	0.906	-0.093	0.405
Galileo-S1X	82.4	0.665	0.851	-0.149	0.640
Galileo-S5X	95.7	0.691	0.842	-0.158	0.681
Galileo-S7X	100.3	0.693	0.842	-0.159	0.685
BDS-S2I	108.9	0.631	0.865	-0.135	0.573
BDS-S6I	140.6	0.636	0.865	-0.136	0.586
BDS-S7I	15.9	0.675	0.853	-0.147	0.624

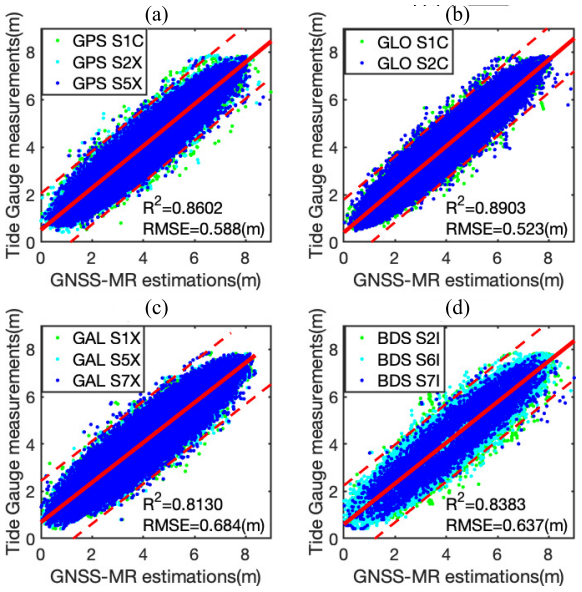

Fig. 8. Correlation analysis charts of tide gauge and GNSS-MR retrievals for (a) GPS, (b) GLONASS, (c) Galileo, and (d) BDS.

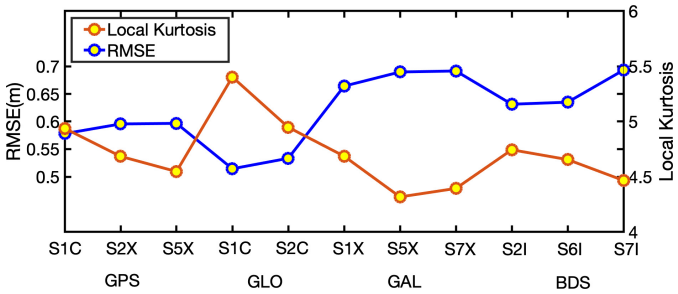

Fig. 9. Comparison of mean LK and RMSE for each SNR type shows a clear negative correlation.

of the tropospheric delay that caused all RH estimations systematically larger than actual values [18]. Therefore, the tropospheric correction in the following steps is extremely important for high precision sea level retrieving.

TABLE IV

COMPARISON OF WEIGHTED ITERATIVE LSM AND ROBUST REGRESSION LSM

	RMSE / m	*Max bias / m*	R^2
Weighted iterative LSM	0.318	2.119	0.9565
Robust regression LSM	0.365	2.116	0.9490

B. Performance of Combined Multi-GNSS

To show the characteristics of the individual signals, the least-square method is used to combine them. As mentioned in Section IV-C, the weight values are determined by a function of LK, and the values of μ and ν in (14) are 1 and 10, respectively, in this article. Fig. 9 shows the comparison of mean LK and RMSE for each SNR type, which shows a clear negative correlation, and thus it is effective to use kurtosis as a weight reference. As shown in Table IV, the RMSE of the weighted iterative LSM result is about 13% lower than that of robust regression LSM mentioned in [28], and the R^2 of the former is larger. Although the max bias of weighted iterative LSM is slightly larger (probably the influence of values with large residuals can be weakened more significantly by the robust regression method), weighted iterative LSM still shows better overall performance.

The final estimations are obtained after the tropospheric correction (the α and β factors in (21) were set to 0.014 and 0.321), Fig. 10(a) shows the final multi-GNSS-MR combined estimations of sea-level h at BRST for each window. The sea levels mostly vary from approximately 1 to 7 m. The large fluctuation amplitude of sea level confirmed the importance of sea-level change rate corrections. The sea-level change rate estimations $\dot{h}$ are given in Fig. 10(b). The change rates are within the range (−2 m/h, 2 m/h), which shows high consistency with h.

Fig. 11 shows the distribution of residuals between multi-GNSS-MR estimations and tide gauge measurements in the whole of 2021. Each grid cell is 1 day along the time axis and 0.05 m along the residual axis. The color indicates the number of estimations in the grid cell. This histogram shows that most

TABLE V
PARAMETERS OF THE SAME TIDAL CONSTITUENTS MONITORED BY TIDE GAUGE AND MULTI-GNSS-MR

		Tide Gauge (Brest)				Multi-GNSS-MR (BRST)				Difference	
Tide	*T(hour)*	*A(cm)*	σ_A*(cm)*	$\varphi(^\circ)$	$\sigma_\varphi(^\circ)$	*A(cm)*	σ_A*(cm)*	$\varphi(^\circ)$	$\sigma_\varphi(^\circ)$	$\lvert\Delta A\rvert$	$\sigma_{\Delta A}$
K1	23.934	0.040	0.014	128.71	25.76	0.039	0.018	127.62	28.45	0.001	0.023
N2	12.658	0.330	0.210	30.63	37.80	0.329	0.208	30.04	34.20	0.001	0.296
M2	12.421	1.325	0.211	7.97	9.25	1.316	0.167	7.11	9.98	0.010	0.269
MKS2	12.385	0.476	0.193	1.81	21.91	0.475	0.178	0.14	21.14	0.001	0.263
2MK6	4.089	0.011	0.005	288.57	33.91	0.011	0.006	6.78	29.04	0.000	0.008

TABLE VI
PARAMETERS OF DIFFERENT TIDAL CONSTITUENTS MONITORED BY TIDE GAUGE AND MULTI-GNSS-MR

Tide Gauge (Brest)						Multi-GNSS-MR (BRST)					
Tide	*T(hour)*	*A(cm)*	σ_A*(cm)*	$\varphi(^\circ)$	$\sigma_\varphi(^\circ)$	*Tide*	*T(hour)*	*A(cm)*	σ_A*(cm)*	$\varphi(^\circ)$	$\sigma_\varphi(^\circ)$
MS4	6.103	0.016	0.010	189.95	33.24	MK4	6.095	0.026	0.013	143.62	30.83
M3	8.280	0.010	0.006	354.05	35.81	MK3	8.177	0.012	0.007	270.47	34.21

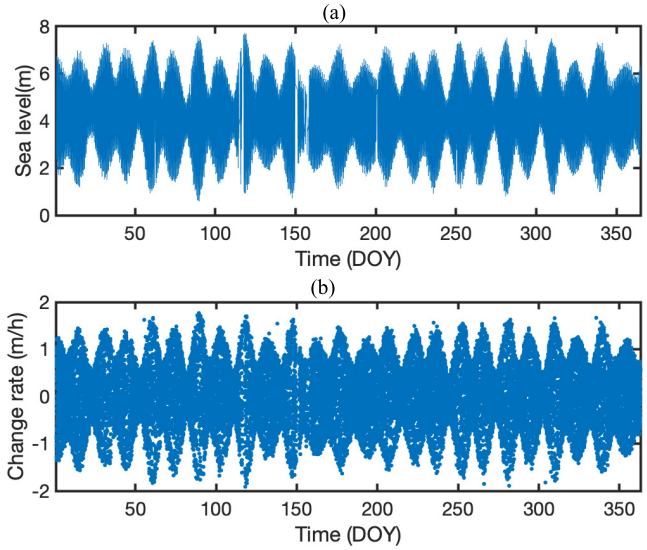

Fig. 10. (a) Final sea-level h estimations. (b) Sea-level change rates estimated by weighted iterative LSM.

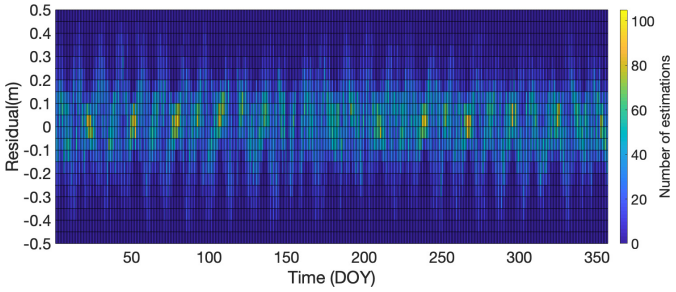

Fig. 11. Distribution of residuals between multi-GNSS-MR estimations and tide gauge measurements of the whole year.

of the large and RH-dependent errors have been effectively weakened, and residuals are mostly within the range (−0.4 m, 0.4 m). The multisignal combined GNSS-MR performed well throughout the year, and the RMSE of the difference between its estimations and tide gauge measurements is 0.134 m, which is much smaller than that of each signal and reduced by 78% on average.

We also plotted correlation analysis diagrams (see Fig. 12) to evaluate the improvement at each step. All retrieved raw data are very scattered and the RMSE reaches 0.610 m. After the weighted iterative LSM combination, the RMSE dropped sharply to 0.318 m and it can be seen from Fig. 12 that the confidence intervals are significantly narrowed. Moving average smoothing further reduced the range of error and continues to decrease the RSME to 0.170 m. Completing the tropospheric delay correction to obtain the final result, the RMSE reached 0.134 m. The correlation coefficient R^2 between multisignal GNSS-MR estimations and tide gauge was also substantially improved from 0.8510 to 0.9917. The slope deviation $(a - 1)$ is also improved from −0.127 to −0.029.

C. Tidal Harmonic Analysis

To analyze the ability of multisignal GNSS-MR to detect different tidal components, a tidal harmonic analysis is performed to compare the sea-level time series obtained by multi-GNSS-MR and by tide gauge. In this step, the MATLAB tool *t_*tide is used to conduct nodal corrections and perform a tidal constituent analysis. The period T, amplitude A, and phase φ are calculated for each tidal constituent. The precision of amplitude σ_A and precision of phase σ_ϕ are estimated for the subsequent comparative analysis. Only tide constituents that meet condition $(A/\sigma_A)^2 > 2$ are assessed as significant

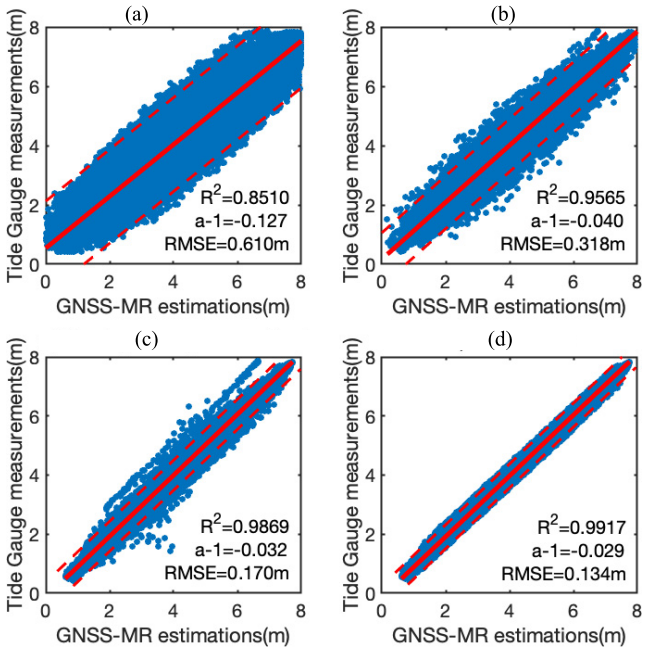

Fig. 12. Correlation analysis diagram of tide gauge and GNSS-MR estimations for all signals, weighted iterative LSM combination, moving average smoothed, and the final result after tropospheric correction. (a) Raw all signals. (b) Weighted iterative LSM. (c) Moving average smoothed. (d) Final result.

constituents, which will be considered in the analysis. The aforementioned parameters of the same tidal constituents in sea-level series obtained by tide gauge and GMSS-MR are presented in Table V. The condition $|\Delta A| > \sigma_{\Delta A}$ is used to evaluate the coincidence of tide gauge and multi-GNSS-MR, and the results indicate that all the shared tides perfectly meet the condition. The different significant tide constituents of tide gauge and multi-GNSS-MR are also listed in Table VI to further analyze the consistency between them. It shows that the difference in the period between MS4–MK4 and M3–MK3 is much less than 10 min, and pairs MS4–MK4 and M3–MK3 fit the condition $|\Delta A| > \sigma_{\Delta A}$ as well. In this case, we can conclude that multi-GNSS-MR has retrieved all daily and subdaily tidal constituents with periods greater than or equal to 10 min.

IV. Conclusion

In this study, we developed a new algorithm to realize multi-GNSS and multisignal combined GNSS-MR sea-level monitoring at a 10-min interval, based on a moving window on SNR time series, weighted iterative LSM, and tropospheric correction. We reduced the RMSE between combined GNSS-MR and tide gauge by 78% on average and improved the correlation to 0.9928, indicating that the estimations are of high quality. Compared with previous research using one or two GNSS systems at BRST station, the precision of combined GNSS-MR sea-level estimation is significantly improved by more than 60% [19], [32], [33]. The main contributions and performances are summarized as follows.

1) Directly windowing on SNR time series significantly increased the number of valid retrievals per day, which generated much more redundant estimations and achieved higher precision by the least-square method even using fewer signals.
2) Weight designing based on LK improved the efficiency of LSM when compared to traditional methods.
3) By making full use of the moving average smoothing and tropospheric correction, the dispersion of error was greatly reduced.

The performances of different GNSS were compared and GLONASS provided the most precise sea-level estimations. Meanwhile, signals of BDS-3 were not fully received, which caused significant observation loss. Therefore, the GNSS receiver should track GLONASS and BDS satellites and make it more convenient for reflectometry applications.

Moreover, this article demonstrated the high performance of multi-GNSS-MR for an entire year and verified its potential applications in tide observations using a tidal harmonic analysis. The result showed that daily and subdaily tide constituents with a period larger than or equal to 10 min can be retrieved precisely using multi-GNSS-MR. Therefore, GNSS-MR can monitor and analyze tidal constituents, which can make up for the deficiency of tide gauges.

Acknowledgment

The authors would like to thank the Global Navigation Satellite System (GNSS) observation and navigation data used here were provided by the International GNSS Service (IGS, ftp://igs.ign.fr/pub/igs/data/highrate/), and the data of the Brest tide gauge are provided by Réseaux de référence des observations marégraphiques (REFMAR, http://data.shom.fr/donnees/refmar).

References

[1] B. Meyssignac and A. Cazenave, "Sea level: A review of present-day and recent-past changes and variability," *J. Geodynamics*, vol. 58, pp. 96–109, Jul. 2012.
[2] G. Griggs, "Rising seas in California—An update on sea-level rise science," in *World Scientific Encyclopedia of Climate Change: Case Studies of Climate Risk, Action, and Opportunity Volume 3*. Singapore: World Scientific, 2021, pp. 105–111.
[3] B. B. Parker, *Tidal Hydrodynamics*. Hoboken, NJ, USA: Wiley, 1991.
[4] G. Feng, S. Jin, and T. Zhang, "Coastal sea level changes in Europe from GPS, tide gauge, satellite altimetry and GRACE, 1993–2011," *Adv. Space Res.*, vol. 51, no. 6, pp. 1019–1028, Mar. 2013.
[5] N. Adebisi, A.-L. Balogun, T. H. Min, and A. Tella, "Advances in estimating sea level rise: A review of tide gauge, satellite altimetry and spatial data science approaches," *Ocean Coastal Manage.*, vol. 208, Jul. 2021, Art. no. 105632.
[6] K. M. Larson, E. E. Small, E. Gutmann, A. Bilich, P. Axelrad, and J. Braun, "Using GPS multipath to measure soil moisture fluctuations: Initial results," *GPS Solutions*, vol. 12, no. 3, pp. 173–177, Jul. 2008.
[7] K. M. Larson, J. S. Löfgren, and R. Haas, "Coastal sea level measurements using a single geodetic GPS receiver," *Adv. Space Res.*, vol. 51, no. 8, pp. 1301–1310, Apr. 2013.
[8] S. Jin, X. Qian, and X. Wu, "Sea level change from BeiDou navigation satellite system-reflectometry (BDS-R): First results and evaluation," *Global Planetary Change*, vol. 149, pp. 20–25, Feb. 2017.
[9] N. Roussel *et al.*, "Sea level monitoring and sea state estimate using a single geodetic receiver," *Remote Sens. Environ.*, vol. 171, pp. 261–277, Dec. 2015.
[10] S. Jin and A. Komjathy, "GNSS reflectometry and remote sensing: New objectives and results," *Adv. Space Res.*, vol. 46, no. 2, pp. 111–117, Jul. 2010.

[11] M. Martín-Neira, "A passive reflectometry and interferometry system (PARIS): Application to ocean altimetry," *ESA J.*, vol. 17, no. 4, pp. 331–355, Dec. 1993.
[12] K. Anderson, "A GPS tide gauge," *GPS World Showcase*, vol. 6, no. 4444, p. 12, 1995.
[13] K. D. Anderson, "Determination of water level and tides using interferometric observations of GPS signals," *J. Atmos. Ocean. Technol.*, vol. 17, no. 8, pp. 1118–1127, Aug. 2000.
[14] A. Bilich and K. M. Larson, "Correction published 29 March 2008: Mapping the GPS multipath environment using the signal-to-noise ratio (SNR)," *Radio Sci.*, vol. 42, no. 6, pp. 1–16, 2007.
[15] S. Tabibi, F. Geremia-Nievinski, and T. van Dam, "Statistical comparison and combination of GPS, GLONASS, and multi-GNSS multipath reflectometry applied to snow depth retrieval," *IEEE Geosci. Remote Sens. Lett.*, vol. 55, no. 7, pp. 3773–3785, Jul. 2017.
[16] A. Santamaría-Gómez and C. Watson, "Remote leveling of tide gauges using GNSS reflectometry: Case study at Spring Bay, Australia," *GPS Solutions*, vol. 21, no. 2, pp. 451–459, 2017.
[17] N. Zheng, P. Chen, and Z. Li, "Accuracy analysis of ground-based GNSS-R sea level monitoring based on multi GNSS and multi SNR," *Adv. Space Res.*, vol. 68, no. 4, pp. 1789–1801, Aug. 2021.
[18] R. N. Treuhaft, S. T. Lowe, C. Zuffada, and Y. Chao, "2-cm GPS altimetry over Crater Lake," *Geophys. Res. Lett.*, vol. 28, no. 23, pp. 4343–4346, 2001, doi: 10.1029/2001GL013815.
[19] S. D. P. Williams and F. G. Nievinski, "Tropospheric delays in ground-based GNSS multipath reflectometry—Experimental evidence from coastal sites," *J. Geophys. Res., Solid Earth*, vol. 122, no. 3, pp. 2310–2327, Mar. 2017, doi: 10.1002/2016JB013612.
[20] X. Qian and S. Jin, "Estimation of snow depth from GLONASS SNR and phase-based multipath reflectometry," *IEEE J. Sel. Topics Appl. Earth Observ. Remote Sens.*, vol. 9, no. 10, pp. 4817–4823, Oct. 2016.
[21] F. G. Nievinski and K. M. Larson, "Forward modeling of GPS multipath for near-surface reflectometry and positioning applications," *GPS Solutions*, vol. 18, no. 2, pp. 309–322, 2014.
[22] K. M. Larson, R. D. Ray, F. G. Nievinski, and J. T. Freymueller, "The accidental tide gauge: A GPS reflection case study from Kachemak Bay, Alaska," *IEEE Geosci. Remote Sens. Lett.*, vol. 10, no. 5, pp. 1200–1204, Sep. 2013.
[23] K. M. Larson, J. J. Braun, E. E. Small, V. U. Zavorotny, E. D. Gutmann, and A. L. Bilich, "GPS multipath and its relation to near-surface soil moisture content," *IEEE J. Sel. Topics Appl. Earth Observ. Remote Sens.*, vol. 3, no. 1, pp. 91–99, Mar. 2010.
[24] N. R. Lomb, "Least-squares frequency analysis of unequally spaced data," *Astrophys. Space Sci.*, vol. 39, no. 2, pp. 447–462, Feb. 1976.
[25] J. D. Scargle, "Studies in astronomical time series analysis. II-statistical aspects of spectral analysis of unevenly spaced data," *Astrophys. J.*, vol. 263, pp. 835–853, Dec. 1982.
[26] X. Wang, Q. Zhang, and S. Zhang, "Water levels measured with SNR using wavelet decomposition and Lomb–Scargle periodogram," *GPS Solutions*, vol. 22, no. 1, p. 22, Jan. 2018.
[27] M. Song, X. He, X. Wang, Y. Zhou, and X. Xu, "Study on the quality control for periodogram in the determination of water level using the GNSS-IR technique," *Sensors*, vol. 19, no. 20, p. 4524, Oct. 2019.
[28] X. Wang, X. He, and Q. Zhang, "Evaluation and combination of quad-constellation multi-GNSS multipath reflectometry applied to sea level retrieval," *Remote Sens. Environ.*, vol. 231, Sep. 2019, Art. no. 111229.
[29] A. Santamaría-Gómez, C. Watson, M. Gravelle, M. King, and G. Wöppelmann, "Levelling co-located GNSS and tide gauge stations using GNSS reflectometry," *J. Geodesy*, vol. 89, no. 3, pp. 241–258, 2015.
[30] O. Montenbruck *et al.*, "The multi-GNSS experiment (MGEX) of the international GNSS service (IGS)—Achievements, prospects and challenges," *Adv. Space Res.*, vol. 59, no. 7, pp. 1671–1697, Apr. 2017.
[31] C. Roesler and K. M. Larson, "Software tools for GNSS interferometric reflectometry (GNSS-IR)," *GPS Solutions*, vol. 22, no. 3, p. 80, Jun. 2018.
[32] X. Wang, Q. Zhang, and S. Zhang, "Azimuth selection for sea level measurements using geodetic GPS receivers," *Adv. Space Res.*, vol. 61, no. 6, pp. 1546–1557, Mar. 2018.
[33] J. S. Löfgren, R. Haas, and H.-G. Scherneck, "Sea level time series and ocean tide analysis from multipath signals at five GPS sites in different parts of the world," *J. Geodynamics*, vol. 80, pp. 66–80, Oct. 2014.

Mingda Ye was born in Jiangxi, China, in 1998. He received the B.Sc. degree from the School of Geodesy and Geomatics, Wuhan University, Wuhan, China, in 2020. He is currently pursuing the M.Sc. degree with the Shanghai Astronomical Observatory, Chinese Academy of Sciences, Shanghai, China.

His research interests include the Global Navigation Satellite System (GNSS)-reflectometry and precise point positioning (PPP) applications.

Shuanggen Jin (Senior Member, IEEE) was born in Anhui, China, in 1974. He received the B.Sc. degree in geodesy from Wuhan University, Wuhan, China, in 1999, and the Ph.D. degree in geodesy from the University of Chinese Academy of Sciences, Beijing, China, in 2003.

He is currently a Professor with Shanghai Astronomical Observatory, CAS, Shanghai, China, and a Vice-President and a Professor at Henan Polytechnic University, Jiaozuo, China. He has published over 500 articles in peer-reviewed journals and proceedings, ten patents/software copyrights, and ten books/monographs with more than 9000 citations and an H-index >50. His main research areas include Satellite Navigation, remote sensing, and space/planetary exploration.

Dr. Jin was an IAG Fellow, an IUGG Fellow, a fellow of the Electromagnetics Academy, a World Class Professor of the Ministry of Education and Cultures, Indonesia, a Chief Scientist of the National Key Research and Development Program, China, a member of the Russian Academy of Natural Sciences, a member of the European Academy of Sciences, a member of Turkish Academy of Sciences, and a member of the Academia Europaea. He received the 100-Talent Program of CAS, Leading Talent of Shanghai. He was the President of the International Association of Planetary Sciences (IAPS) (2015–2019), the President of the International Association of CPGPS (2016–2017), the Chair of the IUGG Union Commission on Planetary Sciences (UCPS) (2015–2023), an Editor-in-Chief of the *International Journal of Geosciences*, the Editor of the *Geoscience Letters*, an Associate Editor of the IEEE TRANSACTIONS ON GEOSCIENCE AND REMOTE SENSING and *Journal of Navigation*, and an Editorial Board Member of *Remote Sensing*, *GPS Solutions*, and *Journal of Geodynamics*.

Yan Jia (Member, IEEE) received the double M.S. degrees in telecommunications engineering and computer application technology from Politecnico di Torino, Turin, Italy, and Henan Polytechnic University, Jiaozuo, China, in 2013. She received the Ph.D. degree in electronics engineering from Politecnico di Torino, in 2017.

In 2013, she joined the Department of Electronics and Telecommunications, Politecnico di Torino. In 2014, she joined the SMAT Project, mainly focusing on the retrieval of soil moisture and vegetation biomass content by Global Navigation Satellite System Reflectometry (GNSS-R). She is currently with the Nanjing University of Posts and Telecommunications, Nanjing, China. Her research interests include microwave remote sensing, soil moisture retrieval, and GNSS-R applications to land remote sensing and antenna design.